

Koopman Autoencoders with Continuous-Time Latent Dynamics for Fluid Dynamics Forecasting

Rares Grozavescu¹ Pengyu Zhang¹ Mark Girolami^{1,2} Etienne Meunier³

Abstract

Data-driven surrogate models have emerged as powerful tools for accelerating the simulation of turbulent flows. However, classical approaches which perform autoregressive rollouts often trade off between strong short-term accuracy and long-horizon stability. Koopman autoencoders, inspired by Koopman operator theory, provide a physics-based alternative by mapping nonlinear dynamics into a latent space where linear evolution is conducted. In practice, most existing formulations operate in a discrete-time setting, limiting temporal flexibility. In this work, we introduce a continuous-time Koopman framework that models latent evolution through numerical integration schemes. By allowing variable timesteps at inference, the method demonstrates robustness to temporal resolution and generalizes beyond training regimes. In addition, the learned dynamics closely adhere to the analytical matrix exponential solution, enabling efficient long-horizon forecasting. We evaluate the approach on classical CFD benchmarks and report accuracy, stability, and extrapolation properties.

1. Introduction

Simulating turbulent flows is a fundamental problem in fluid dynamics, with applications ranging from aerodynamics and weather prediction to engineering design. Traditional computational models such as Direct Numerical Simulation (DNS), Large-Eddy Simulation (LES), and Reynolds-averaged Navier–Stokes (RANS) (Ghasemian et al., 2017; Slotnick et al., 2014) are extremely expensive in both computation and memory, especially for long time horizons or high-resolution domains. This motivates the development of data-driven surrogate models that can efficiently forecast

¹Department of Engineering, University of Cambridge, Cambridge, UK ²Alan Turing Institute, London, UK ³Inria, Paris, France. Correspondence to: Rares Grozavescu <rg625@cam.ac.uk>.

complex unsteady flows.

Deep learning has recently emerged as a promising tool for flow prediction (Borrelli et al., 2022; Srinivasan et al., 2019; Fukami et al., 2020; Morimoto et al., 2021). Classical data-driven solvers operate directly on the data space, mapping flow fields at the current timestep to the next autoregressively using deep learning models such as Convolutional Neural Networks (CNNs) (Krizhevsky et al., 2012), Graph Neural Networks (GNNs) (Kipf & Welling, 2017) and Neural Operators (Lu et al., 2021; Li et al., 2021). While such data-space models excel at capturing fine-scale features, they tend to suffer from error accumulation, high computational cost due to step-by-step rollouts, and reduced stability over long horizons.

Alternatively, latent-space models compress high-dimensional flow fields into low-dimensional embeddings and evolve them over time using different network structures. LE-PDE, proposed by Wu et al. (2022), illustrates that learning the evolution of dynamics in a global latent space is a simple, fast and scalable method to accelerate the simulation. Within the latent space paradigm, a class of physics-based methods based on Koopman theory (Koopman, 1931) has been proposed. Koopman theory states that the nonlinear dynamics of a system could be represented as an infinite-dimensional linear operator, known as the Koopman operator. By linearizing the dynamics, Koopman theory enables the use of spectral analysis and linear algebra to study nonlinear dynamics. However, identifying the Koopman operator is challenging due to its infinite-dimensional nature. One classical approach is Dynamic Mode Decomposition (DMD) (Kutz et al., 2016), which estimates finite-dimensional approximations of the Koopman operator directly from data. To improve its expressive power, Takeishi et al. (2017) extended DMD by introducing neural networks to learn nonlinear feature maps, enabling Koopman operator estimation in a learned feature space. Building on this line of work, Lusch et al. (2018) proposed an encoder-decoder architecture, forming the basis of Koopman Autoencoders (KAEs).

Latent-space evolution reduces computational cost and improves long-term stability, but most existing approaches rely on discrete-time updates, which can limit flexibility and

temporal generalization. While effective, this formulation constrains the model to the sampling resolution of training data and can hinder extrapolation across different timesteps. Inspired by recent advances in neural ODEs, we propose to use a continuous-time update for latent space evolution. By modelling the latent dynamics through an ODE and integrating them with stable numerical schemes, our approach decouples the learned dynamics from fixed time intervals, enabling flexible rollouts, improved robustness, and principled generalization across temporal scales. We compare our proposed methodology with a benchmark work using conditional diffusion models (Kohl et al., 2026) in terms of accuracy and efficiency. Our contributions are summarized below.

Contributions:

- **Continuous-Time Koopman Autoencoder:** We introduce a Koopman autoencoder framework where latent dynamics are modeled in continuous time, enabling stable and flexible temporal evolution beyond the training timestep.
- **Physics-Informed, Parameter-Dependent Latent Dynamics:** The latent Koopman operator is conditioned on physical parameters (e.g., Reynolds or Mach numbers), allowing the model to generalize across different flow regimes while maintaining physically consistent predictions.
- **Latent Dynamics Consistency:** We demonstrate that the learned latent dynamics closely match the analytical solution via matrix exponentiation, enabling efficient and accurate long-horizon forecasting without iterative rollouts.
- **Efficiency and Robustness:** Our approach significantly reduces computational cost compared to autoregressive diffusion models, while supporting zero-shot generalization across variable timesteps.

2. Related Work

Autoregressive prediction in data space. Classical deep learning approaches for flow forecasting adopt autoregressive prediction in the data space. CNNs, particularly U-Net architectures (Ronneberger et al., 2015), have been widely used to capture spatial features in an image-to-image translation framework (Deo et al., 2023; Wang et al., 2019). Other approaches have also explored generative models. For instance, Generative Adversarial Networks (GANs) (Goodfellow et al., 2020) have been employed to predict complex unsteady flow dynamics around objects like cylinders (Lee & You, 2019). Similarly, conditional diffusion models (Batzolis et al., 2021) have been benchmarked for their ability

to predict turbulent flow simulations autoregressively (Kohl et al., 2026).

Latent-space autoregressive models. Many works compress flow fields into a latent representation and evolve it autoregressively. This approach decouples the spatial complexity from the temporal dynamics. Classical examples include CNN autoencoders coupled with LSTMs (Hochreiter & Schmidhuber, 1997) and Recurrent Neural Networks (RNNs) to propagate the latent state forward in time (Eivazi et al., 2020; Hasegawa et al., 2020; Bukka et al., 2020; Maulik et al., 2021; Zhou & Cheng, 2025). Similarly, Graph Neural Networks (GNNs) have proven effective for systems with irregular geometries to conduct temporal evolution in latent space (Sanchez-Gonzalez et al., 2020). More recently, transformers (Vaswani et al., 2017) have also been adapted for this task, leveraging its powerful attention mechanism to capture long-range temporal dependencies in the latent dynamics of fluid flows (Hemmasian & Farimani, 2023).

Koopman autoencoders. Building upon (Lusch et al., 2018)’s foundational work, subsequent studies have introduced enhancements. Azencot et al. (2020) proposed Consistent Koopman Autoencoders, integrating both forward and backward dynamics and enhancing accuracy for long time predictions. Temporally-Consistent Koopman Autoencoder (tcKAE) (Nayak et al., 2025) achieved accurate long-term predictions with limited and noisy training data through a consistency regularization term. Halder et al. (2026) proposed Koopman β -variational autoencoders for reduced-order modeling (ROM) of turbulent flows. K^2 VAE integrates KalmanNet with KAEs to refine predictions and model uncertainty (Wu et al., 2025).

3. Background

3.1. Koopman Autoencoders

Koopman operator theory provides a linear perspective on nonlinear dynamics. Consider a discrete-time dynamical system with states $x_t \in \mathbb{R}^{N_d}$, where x_t denotes the state of the system at time $t \in N$. The state evolves to its next timestep $t + \Delta t$ according to a flow map $f : \mathbb{R}^{N_d} \rightarrow \mathbb{R}^{N_d}$:

$$x_{t+\Delta t} = f(x_t). \quad (1)$$

Koopman operator theory shifts the focus from the state variables x_t to a set of measurement functions $h : \mathbb{R}^{N_d} \rightarrow \mathbb{R}$, which are elements of an infinite-dimensional Hilbert space. The Koopman operator \mathcal{K} acts on measurement functions h linearly with the dynamics:

$$(\mathcal{K}h)(x_t) = h(f(x_t)) = h(x_{t+\Delta t}). \quad (2)$$

In this formulation, the underlying nonlinear system (1) is transformed into a linear evolution in the infinite-dimensional space of observables. The challenge lies in

choosing or constructing a suitable set of observables. KAEs address this by learning the observables from data, training an encoder which maps the state into a latent representation $\mathcal{E} : \mathbb{R}^{N_d} \rightarrow \mathbb{R}^{N_z}$,

$$z_t = \mathcal{E}(x_t), \quad (3)$$

which approximates the set of observables $h(x_t)$. In this latent space, the evolution can be modelled as an approximately linear finite-dimensional Koopman operator \mathbf{K} ,

$$z_{t+\Delta t} \approx \mathbf{K}z_t. \quad (4)$$

A decoder \mathcal{D} then reconstructs the state from latent variables,

$$\hat{x}_{t+\Delta t} = \mathcal{D}(z_{t+\Delta t}). \quad (5)$$

While most KAE formulations operate in discrete time, directly mapping $z_t \rightarrow z_{t+\Delta t}$, such updates are tied to the temporal resolution of training data. This dependence can hinder generalization across timesteps and reduce robustness in scenarios with different or irregular temporal resolutions. To overcome this limitation, we propose continuous-time variants which treat latent dynamics as an ODE:

$$\frac{dz}{dt} = \mathbf{K}z, \quad (6)$$

which naturally accommodates variable timesteps, enabling variable-step integration and extrapolation beyond training timescales.

3.2. Numerical Integration and Latent Dynamics

In contrast to Neural ODEs which model dynamics using black-box models, our approach restricts latent dynamics to a linear form, thereby aligning with the linear latent dynamics described by Koopman theory. This linearity also enables precise state evolution through matrix exponentiation, yielding efficient long-horizon forecasting.

Linear Stability and Integration. In our method, we need to choose a numerical integration scheme for state evolution. Forward Euler integrators are simple to implement and interpret, however, they tend to diverge unless the integrator step is small enough, thus making them unpractical. Among available choices, the classical fourth-order Runge–Kutta (RK4) method offers a strong balance of accuracy, stability and interpretability, making it particularly suitable for long-rollout predictions.

Integration via Matrix Exponentiation. During inference time, we can leverage the analytical solution of the learned linear system to bypass iterative solvers entirely. Given the linear system in (6), the exact solution for any future state z_τ given z_0 is defined by the matrix exponential $z_\tau = \exp(\mathbf{K}\tau)z_0$, where we can predict the state at arbitrary time τ directly, independent of the step size Δt . The

matrix exponential $\exp(\mathbf{M})$ is defined by power series:

$$\exp(\mathbf{M}) = \sum_{n=0}^{\infty} \frac{\mathbf{M}^n}{n!} = \mathbf{I} + \mathbf{M} + \frac{\mathbf{M}^2}{2!} + \frac{\mathbf{M}^3}{3!} + \dots \quad (7)$$

4. Method

In this section, we present the methodology of our proposed continuous-time KAE. We begin by defining the network architecture. We then detail the mathematical formulation of our proposed framework. Finally, we outline the training strategy.

4.1. Proposed Model

The proposed KAE consists of three main components: a dual-stream Transformer encoder, a parametric latent Koopman operator, and a CNN-based decoder. More details on the exact implementation can be found in Appendix B.1.

Let $x_t \in \mathbb{R}^{N_d}$ denote the high-dimensional physical state of the system. We assume the data is at discrete timestamps t_i , which are uniformly spaced by a fixed time interval Δt , such that $t_{i+1} = t_i + \Delta t$. Accordingly, x_{t_i} represents the state snapshot at time t_i .

4.1.1. ENCODER AND DECODER

We employ a Transformer-based encoding architecture which is split into two streams: a history encoder ($\mathcal{E}_{\text{history}}$) and a present encoder ($\mathcal{E}_{\text{present}}$). The history encoder is designed to process a sequence of past states. While the architecture supports an arbitrary number of previous steps, for consistency with benchmark evaluations, we employ an Auto-Regressive order of 2 (AR-2). Suppose the current state is x_{t_i} , the history encoder conditions only on the immediate past state $x_{t_{i-1}}$. The present encoder processes the current state x_{t_i} . The initial latent state z_{t_i} is constructed by taking the average of outputs from two encoders,

$$z_{t_i} = \frac{1}{2} (\mathcal{E}_{\text{present}}(x_{t_i}) + \mathcal{E}_{\text{history}}(x_{t_{i-1}})). \quad (8)$$

A decoder \mathcal{D} reconstructs the physical state from the latent vector, $\hat{x}_{t_i} = \mathcal{D}(z_{t_i})$.

4.1.2. KOOPMAN OPERATOR

Next, we discuss the structure of the Koopman operator. A key innovation in our approach is the dependence of the Koopman operator on external control parameters, denoted by ϕ . In physical systems, such as turbulent flows, ϕ may represent the Reynolds number or other governing coefficients. Unlike traditional Koopman approaches where the operator is constant across the domain, our operator varies based on the physical regime.

Our proposed continuous-time model interprets the latent evolution as an ODE,

$$\frac{dz}{dt} = \mathbf{K}_{\text{cont}}(\phi)z, \quad (9)$$

where \mathbf{K}_{cont} governs the linear evolution in latent space. The state at a future time, $t_i + \Delta t$, is obtained by integrating this ODE:

$$z_{t_i + \Delta t} = z_{t_i+1} = z_{t_i} + \int_0^{\Delta t} \frac{dz}{dt} dt, \quad (10)$$

where RK4 integration is used.

Finally, we define the structure of the operator. To capture the dependency on physical parameters ϕ , we express $\mathbf{K}_{\text{cont}}(\phi)$ as the sum of a static base dynamics and a parametric adjustment:

$$\mathbf{K}_{\text{cont}}(\phi) = \mathbf{K}_0 + \mathcal{N}_\psi(\phi). \quad (11)$$

Here, the base dynamics are governed by a learnable matrix \mathbf{K}_0 , which captures the global behavior shared across the systems. \mathcal{N}_ψ is Low-Rank Adaptation (LoRA (Hu et al., 2022)) parameterized by ψ , and it predicts the regime-specific deviations induced by ϕ and outputs a correction matrix matching the shape of \mathbf{K}_0 .

4.2. Training

The training procedure follows a recurrent rollout scheme. Given an input sequence context $\{x_{t_{i-1}}, x_{t_i}\}$, the model predicts a future trajectory of length N , denoted as $\{\hat{x}_{t_{i+1}}, \hat{x}_{t_{i+2}}, \dots, \hat{x}_{t_{i+N}}\}$. An architecture overview is provided in Figure 1, detailing the introduction of initial latent states, the latent dynamics propagation and how each of the states can be independently mapped back to the original data space.

The training objective is defined as a weighted combination of several loss components that enforce accurate reconstruction, long-horizon prediction, latent-space consistency, and physics-informed regularization. All losses are computed as mean squared errors (MSE) unless stated otherwise.

Reconstruction loss. The reconstruction loss enforces consistency between the reconstructed initial state produced by the decoder and the corresponding ground-truth state. Let $\mathbf{x}_{t_i} = \{x_{t_i,q}\}_{q \in \mathcal{Q}}$ denote the flow states at time t_i , decomposed into its physical components (e.g. velocity components, pressure), where \mathcal{Q} indexes the set of state variables shared by the prediction and ground-truth representations. The reconstruction loss is defined as

$$\mathcal{L}_{\text{recon}} = \sum_{q \in \mathcal{Q}} \mathbb{E}_{x \sim p(\text{data})} \left[\|\hat{x}_{t_i,q} - x_{t_i,q}\|_2^2 \right], \quad (12)$$

where $x \sim p(\text{data})$ denotes the empirical data distribution induced by the training dataset.

Rollout prediction loss. The rollout prediction loss penalizes errors over future time steps produced by iterating the learned latent dynamics and decoding the resulting latent states,

$$\mathcal{L}_{\text{pred}} = \sum_{q \in \mathcal{Q}} \mathbb{E}_{x \sim p(\text{data})} \left[\sum_{j=1}^N w_{i+j} \|\hat{x}_{t_{i+j},q} - x_{t_{i+j},q}\|_2^2 \right], \quad (13)$$

where N is the rollout horizon and $\{w_{i+j}\}_{j=1}^N$ are normalized temporal weights. In this work, the weights are either uniform or follow a cosine schedule that emphasizes early prediction accuracy,

$$w_{i+j} \propto \frac{1}{2} \left(1 + \cos \left(\frac{\pi(i+j-1)}{N-1} \right) \right). \quad (14)$$

Latent consistency loss. To encourage consistency between the predicted latent trajectory and the latent representations obtained by encoding the ground-truth states, we include a latent-space loss,

$$\mathcal{L}_{\text{latent}} = \mathbb{E}_{x \sim p(\text{data})} \left[\sum_{j=1}^N \|z_{t_{i+j}} - \mathcal{E}_{\text{present}}(x_{t_{i+j}})\|_2^2 \right], \quad (15)$$

where z_{t_i} denotes the latent state obtained by rolling out the latent dynamics, and $\mathcal{E}_{\text{present}}(\cdot)$ is the encoder network.

Physics-informed regularization. In addition to the standard reconstruction and prediction losses, we include physics-inspired penalties that improve temporal alignment and structural fidelity of long rollouts. These include: (i) a temporal Sobolev loss matching finite-difference time derivatives, (ii) a spatial gradient loss enforcing edge and structure consistency, and (iii) a spectral loss computed in the Fourier domain to penalize frequency and phase mismatches. All physics terms are aggregated into a single auxiliary loss $\mathcal{L}_{\text{phys}}$. More details can be found in Appendix C.

Overall objective. The final training objective is given by

$$\mathcal{L}_{\text{total}} = \mathcal{L}_{\text{recon}} + \alpha \mathcal{L}_{\text{pred}} + \beta \mathcal{L}_{\text{latent}} + \lambda_{\text{phys}} \mathcal{L}_{\text{phys}}, \quad (16)$$

where α and β control the relative contributions of the rollout prediction and latent consistency losses, respectively, and λ_{phys} weights the optional physics-informed regularization terms.

5. Datasets

We compare our model with the benchmarking Autoregressive Conditional Diffusion Models (ACDM) (Kohl et al., 2026) and use the same dataset they generate for training and evaluation as well. We use two scenarios of flow in the dataset, an incompressible wake flow and a transonic cylinder flow with shock waves.

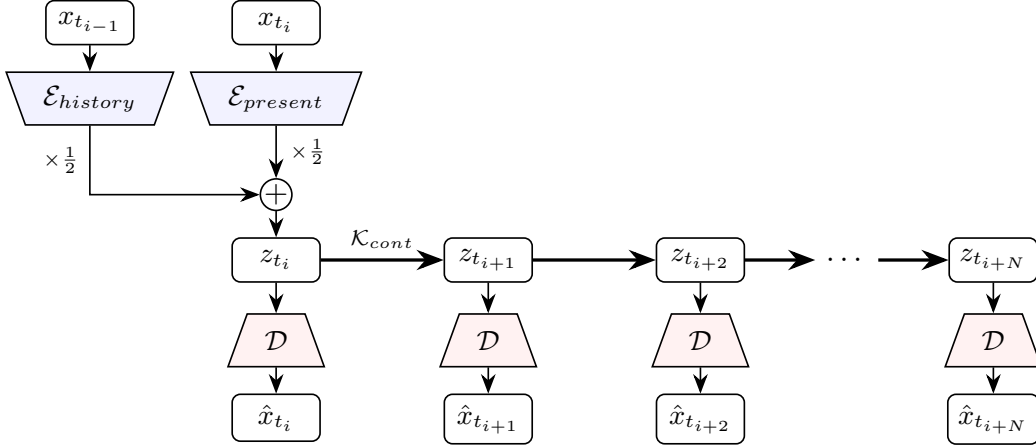


Figure 1. Architecture overview. The history encoder and present encoder (top) feed into the latent state z_{t_0} , followed by a dynamics rollout and decoding at each step.

Incompressible Wake Flow. This dataset consists of a fully developed incompressible Karman vortex street behind a cylindrical obstacle with varying Reynolds numbers $Re \in [100, 1000]$, with 91 simulations in total. For training, both ACDM and our model utilize simulations within the range $Re \in [200, 900]$. There are two distinct test sets: Inc_{low} , covering $Re \in [100, 180]$, and Inc_{high} , covering $Re \in [920, 1000]$, with a prediction horizon of $T = 60$ steps. While the raw datasets employ a time step of $\Delta t = 0.05\text{s}$, we follow the baseline protocol and subsample the trajectories by a factor of 2, resulting in an effective time step of $\Delta t = 0.1\text{s}$ for model training and evaluation.

Transonic Cylinder Flow. Transonic flows are more chaotic, exhibiting the formation of shock waves that interact with the flow. The dataset consists of 40 sequences of fully developed compressible Karman vortex streets at a fixed Reynolds number $Re = 10,000$, with Mach numbers varying across the range $Ma \in [0.50, 0.90]$. Both models are trained on sequences with $Ma \in [0.53, 0.63] \cup [0.69, 0.90]$. Two of the testsets Tra_{ext} and Tra_{int} represent simulations with $Ma \in [0.50, 0.52]$ and $Ma \in [0.66, 0.68]$ respectively with rollout steps $T = 60$, and another long rollout case of about 8 vortex shedding periods, Tra_{long} , has $Ma \in [0.64, 0.65]$ and $T = 240$. Similar to the incompressible case, the raw simulation interval is $\Delta t = 0.05\text{s}$, which is subsampled to $\Delta t = 0.1\text{s}$ for our experiments.

6. Experiments

In this section, we present a comprehensive evaluation of our proposed method. First, we detail the **Experimental Setup**, contrasting our training strategies with ACDM baseline to highlight key methodological differences. Subsequently, we report the **Results**, assessing the model’s performance on

incompressible and transonic flows.

6.1. Experimental Setup

While we utilize the same underlying data as the ACDM baseline, we introduce specific methodological refinements to the training protocol to maximize data efficiency and ensure a rigorous comparison. All models were trained to forecast the next $N = 8$ states conditioned on the present one and the previous one.

Data Loading Strategy: Standard training of ACDM utilizes non-overlapping sequences to form training batches. This approach discards a significant portion of valid temporal transitions. In contrast, we adopt an exhaustive sliding-window strategy, where we generate training batches by sliding the window forward by a single time step. This implies that if a sequence begins at t_i , the next valid training sequence begins at t_{i+1} . This strategy significantly increases the effective dataset size and forces the encoder to learn a more robust, temporally consistent manifold.

Loss Function Formulation: The probabilistic nature of the diffusion baseline constrains its objective function to a simple MSE objective derived from the Gaussian diffusion assumption. Our deterministic framework allows for a composite loss function (as defined in (16)) that incorporates physics-informed constraints, leading to sharper structural predictions.

Training Regimes: ACDM baseline for the Incompressible Flow dataset was trained on the fully developed regime. While effective for capturing stationary statistics, this protocol excludes the initial transient phase where the flow develops from rest. To ensure a rigorous comparison of generalization capabilities, we define two distinct evaluation

settings:

- **Stable-Only Training:** Models are trained only on the fully developed regime. This includes the original baseline ($ACDM$), its no-noise-conditional alternative ($ACDM_{ncn}$), and our standard model (*Continuous KAE*).
- **Full-Dataset Training:** Models are trained on the complete evolution history, including the transient initialization. We retrained the baseline from scratch on the full dataset (*Full retrained $ACDM$*) and compare it against our *Full Continuous KAE* model.

Note that for the Transonic Flow, all models (baseline and ours) were trained on the full dataset by default.

6.2. Results

We structure our evaluation into four main parts: a quantitative analysis comparing our method against baselines, a validation of the learned integrator against the analytical matrix exponential, an assessment of temporal consistency across varying resolutions, and a final study on computational efficiency.

Quantitative Analysis. Table 1 illustrates the results of five distinct models evaluated on the full Incompressible Flow dataset. The comparison reveals that the three models trained exclusively on the fully developed regime exhibit significantly higher MSE, primarily due to their lack of exposure to the initial transient dynamics. Most notably, our *Full Continuous KAE* outperforms *Full retrained $ACDM$* in both Inc_{low} and Inc_{high} .

Table 3 details the quantitative performance evaluated on fully developed Incompressible Flow and full dataset of Transonic Flow. Our *continuous KAE* achieves predictive accuracy highly competitive with $ACDM$ baseline, yielding MSE and LSIM scores effectively comparable with $ACDM$. Figure 2 further provides a visual comparison of rollout predictions on Inc_{high} and Tra_{ext} , where t denotes the number of autoregressive steps (corresponding to physical time $t \cdot \Delta t$). Notably, the chaotic nature of the transonic flow proves challenging for long-horizon forecasting, with both $ACDM$ and *Continuous KAE* starting to exhibit visible error accumulation and divergence from the ground truth at around step $t = 45$.

Integrator Analysis. We compare the trajectories generated by the numerical RK4 integrator against the analytical matrix exponential solution derived in Section 3.2 at inference time. Results are shown in Figure 3 and the final two rows of Table 3. While RK4 performs iterative rollouts with a fixed step $\Delta t = 0.1s$, the analytical formulation allows

us to directly compute $z_\tau = \exp(\mathbf{K}\tau)z_0$ for any target time τ . In Figure 3, t denotes the number of rollout steps, corresponding to a physical time $\tau = t \cdot \Delta t$. Both Figure 3 and Table 3 show perfect alignment with two methods. This allows for highly efficient long-horizon forecasting, because to predict a frame far into the future, one can simply utilize the matrix exponential form to compute the state in a single step, bypassing the computational overhead of iterative integration.

Temporal Consistency and Generalization. A key advantage of our *continuous-time KAE* is its ability of zero-shot temporal generalization. Despite being trained on a fixed timestep $\Delta t = 0.1s$, the model supports arbitrary integration step sizes during inference. We validate this capability in Figure 4, which displays rollouts generated using three distinct integration step sizes, $\Delta t \in \{0.05s, 0.1s, 0.2s\}$. For each case, the number of rollout steps is adjusted to align with the same set of physical time instants (up to $t = 2.0s$). The first row also shows the results produced using the analytical exponential form. The perfect alignment confirms that the learned dynamics are robust to discretization changes.

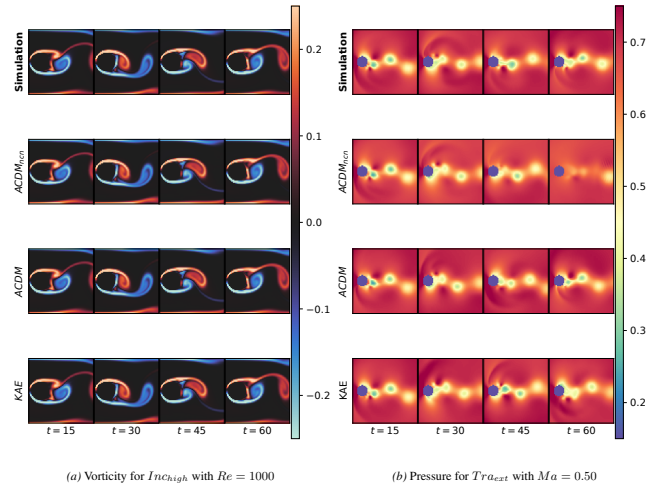


Figure 2. Qualitative validation rollouts for extrapolation regimes. (Left) Vorticity prediction for the incompressible wake flow in the high-Reynolds-number regime (Inc_{high} , $Re = 1000$). (Right) Pressure prediction for the transonic cylinder flow in the low-Mach extrapolation regime (Tra_{ext} , $Ma = 0.50$).

Efficiency. Table 2 presents a comprehensive comparison of computational performance between the diffusion-based $ACDM$ model and our continuous-time KAE. The KAE demonstrates dramatic runtime improvements: encoding and decoding operations require only a few milliseconds per frame, while a full 240-step rollout is executed in approximately $1.2ms$, corresponding to a per-step cost of $1.67\mu s$. In contrast, $ACDM$ exhibits rollout times exceeding $340ms$,

Method	Inc_{low}		Inc_{high}	
	MSE ($\times 10^{-4}$)	LSiM ($\times 10^{-2}$)	MSE ($\times 10^{-5}$)	LSiM ($\times 10^{-2}$)
$ACDM_{ncn}$	175.1 ± 14.3	73.3 ± 4.4	2348.3 ± 291.3	82.5 ± 4.0
$ACDM$	8.5 ± 19.2	12.6 ± 14.9	223.3 ± 614.2	10.4 ± 21.7
Full retrained $ACDM$	1.4 ± 1.7	6.2 ± 4.6	2.4 ± 1.9	1.9 ± 0.5
Continuous KAE	9.2 ± 20.9	13.2 ± 16.3	213.7 ± 457.6	12.6 ± 22.3
Full Continuous KAE	1.0 ± 1.3	5.2 ± 4.4	1.4 ± 2.6	1.0 ± 0.7

Table 1. Quantitative comparison on incompressible wake flow extrapolation regimes (Inc_{low} and Inc_{high}). Performance is reported using MSE and LSiM (where lower values indicate better performance), averaged over rollout timesteps. Simple $ACDM$ and $ACDM_{ncn}$, as well as *Continuous KAE*, were trained only on the fully developed regime, whereas the Full retrained models were trained on the full dataset.

Action / Metric	$ACDM$	KAE
Encode (ms $\times 10^{-1}$)	–	2.44
Decode (ms $\times 10^{-2}$)	–	3.56
240-step rollout (ms $\times 10^{-1}$)	341.42	1.21
Latent avg./step (ms $\times 10^{-4}$)	–	5.06
Total avg./step (ms $\times 10^{-3}$)	142.26	1.67

Table 2. Comprehensive runtime comparison between $ACDM$ and *continuous KAE* across a 240-step rollout. The table is split into two parts for clarity: the top table presents the breakdown of KAE runtimes by model components (Encode, Decode) alongside the total 240-step rollout time, allowing a direct comparison of per-component computational overhead. The bottom table reports derived per-step metrics, including the average computation time per step and the total average per-step time across the rollout, which are more directly indicative of the model’s efficiency in long-horizon predictions. All values are reported as mean \pm standard deviation in milliseconds (ms) across multiple independent runs.

yielding over $300\times$ slower long-horizon predictions. These results highlight that, by leveraging a latent linear dynamics formulation, the KAE achieves both high accuracy and orders-of-magnitude faster inference, making it particularly suitable for large-scale or real-time spatiotemporal simulations.

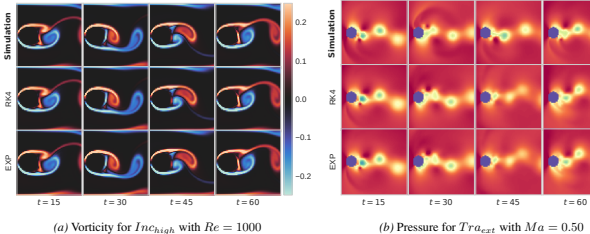


Figure 3. Comparison between numerical RK4 integration and the analytical matrix exponential solution of the learned continuous-time latent dynamics. Results are shown for (Left) incompressible flow vorticity at $Re = 1000$ and (Right) transonic flow pressure at $Ma = 0.50$.

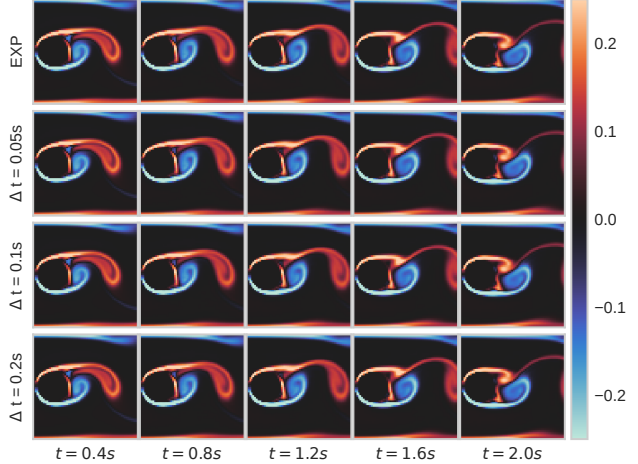


Figure 4. Direct comparison of inference results using the matrix exponentiation and integrator at different time steps. All columns display the flow’s evolution at the same physical time and each row represents a different evolution scheme: first one is the direct matrix exponentiation, while the subsequent ones use the RK4 integrator with different time steps.

7. Discussion

In this work, we presented a continuous-time Koopman Autoencoder that effectively decouples the learning of latent dynamics from the temporal resolution of the training data. Our results on incompressible and transonic flows demonstrate that this approach offers a compelling alternative to state-of-the-art probabilistic methods like $ACDM$.

Accuracy vs. Efficiency Trade-off. While diffusion models such as $ACDM$ excel at capturing high-frequency texture through stochastic refinement, they incur a significant computational cost during inference due to iterative denoising steps. Our method, by contrast, utilizes a deterministic ODE solver in the latent space. As shown in Table 1, our continuous formulation achieves competitive MSE and LSiM scores, often within the error margins of $ACDM$, while being two orders of magnitude faster during inference. This efficiency is critical for real-time control and design optimization loops.

Convergence Speed. As a result of the exhaustive data loading and the deterministic nature of our model, we achieve convergence significantly faster than the baseline. Our models are trained for 200 epochs, whereas $ACDM$ requires 1000 epochs.

Temporal Generalization. A key advantage of the continuous-time formulation is robustness to temporal resolution. Our model maintains physical consistency when queried at time intervals different from training. Crucially, when the learned latent dynamics are evolved using the analytical matrix exponentiation, predictions remain stable

Method	Inc_{low}		Inc_{high}		Tra_{ext}		Tra_{int}		Tra_{long}^*	
	MSE ($\times 10^{-4}$)	LSiM ($\times 10^{-2}$)	MSE ($\times 10^{-5}$)	LSiM ($\times 10^{-2}$)	MSE ($\times 10^{-3}$)	LSiM ($\times 10^{-1}$)	MSE ($\times 10^{-3}$)	LSiM ($\times 10^{-1}$)	MSE ($\times 10^{-3}$)	LSiM ($\times 10^{-1}$)
Λ CDM _{ncn}	0.9 ± 0.8	6.6 ± 2.7	5.7 ± 2.7	3.6 ± 1.2	4.1 ± 1.9	1.9 ± 0.6	2.8 ± 1.3	1.7 ± 0.4	22.2 ± 3.8	8.2 ± 3.0
Λ CDM	1.7 ± 2.2	6.9 ± 5.6	0.8 ± 0.4	1.0 ± 0.3	2.3 ± 1.4	1.3 ± 0.3	2.7 ± 2.1	1.3 ± 0.6	22.3 ± 4.6	3.8 ± 0.4
Continuous KAE	1.3 ± 1.7	6.1 ± 4.8	2.9 ± 1.1	1.7 ± 0.3	2.5 ± 0.8	1.8 ± 0.3	6.5 ± 1.6	2.2 ± 0.4	17.0 ± 2.3	4.1 ± 0.3
Exponential Continuous KAE	1.3 ± 1.7	6.1 ± 4.8	2.9 ± 1.1	1.7 ± 0.3	2.5 ± 0.8	1.8 ± 0.3	6.5 ± 1.6	2.2 ± 0.4	17.0 ± 2.3	4.1 ± 0.3

Table 3. Quantitative comparison across incompressible and transonic flow regimes, including extrapolation (Inc_{low} , Inc_{high} , Tra_{ext} , Tra_{int}) and long-horizon rollout (Tra_{long}). Metrics reported are MSE and LSiM. Results for Tra_{long} are computed by the authors, as this setting is not reported in the original Λ CDM paper.

and closely match those obtained via numerical integration of RK4. This demonstrates that the model learns a valid continuous-time generator of the dynamics, enabling zero-shot evaluation at arbitrary temporal resolutions. In contrast, discrete-time baselines typically fail under such temporal mismatches or require retraining, indicating reliance on step-to-step mappings rather than an underlying dynamical operator.

Limitations. Despite these successes, we observe that the spectral bias of the L_2 reconstruction loss can lead to the smoothing of fine-scale turbulent features over very long horizons, a common issue in deterministic autoencoders. Additionally, while the Koopman operator provides interpretability, the assumption of global linearity (even with residual corrections) remains a constraint for highly nonlinear phenomena like shock wave propagation in the transonic regime. We also noted that stabilizing the training of the operator requires careful curriculum learning and spectral normalization, indicating a sensitivity to hyperparameter tuning.

8. Conclusion

We have introduced a Koopman Autoencoder with continuous-time latent dynamics for data-driven fluid dynamics forecasting. By modeling the evolution of flow fields as an ODE in a compressed latent space, our approach combines the theoretical grounding of Koopman operator theory with the flexibility of neural differential equations. We demonstrated that integrating these dynamics with a fourth-order Runge-Kutta scheme allows for accurate, stable, and resolution-invariant predictions across incompressible and transonic flow regimes.

Our extensive benchmarks against conditional diffusion models highlight that continuous-time KAEs can match state-of-the-art accuracy while offering superior computational efficiency and temporal generalization. Future work will focus on scaling this approach to three-dimensional turbulence and incorporating explicit conservation laws into the latent ODE structure to further improve long-term physical fidelity.

Impact Statement

This paper presents a method for accelerating the simulation of complex fluid dynamics, which has broad applications in engineering, climate science, and energy sectors. By providing a surrogate model that is orders of magnitude faster than traditional numerical solvers (DNS/LES), this work contributes to more energy-efficient computational workflows, reducing the carbon footprint associated with high-performance computing.

In engineering contexts, such as aerodynamic design or wind energy optimization, faster simulation tools can accelerate the development of efficient technologies. We do not foresee immediate negative ethical consequences or societal risks associated with this specific algorithmic contribution.

Software and Data

Datasets are detailed at <https://github.com/tum-pbs/autoreg-pde-diffusion/tree/main>. These data sets are available at the training and evaluation resolution of 128×64 (about 146 GB).

References

- Azencot, O., Erichson, N. B., Lin, V., and Mahoney, M. W. Forecasting sequential data using consistent koopman autoencoders. In *Proceedings of the 37th International Conference on Machine Learning*, ICML’20, 2020.
- Batzolis, G., Stanczuk, J., Schönlieb, C.-B., and Etmann, C. Conditional image generation with score-based diffusion models. *arXiv preprint arXiv:2111.13606*, 2021.
- Borrelli, G., Guastoni, L., Eivazi, H., Schlatter, P., and Vinuesa, R. Predicting the temporal dynamics of turbulent channels through deep learning. *International Journal of Heat and Fluid Flow*, 96:109010, 2022.
- Bukka, S. R., Magee, A. R., and Jaiman, R. K. Deep convolutional recurrent autoencoders for flow field prediction. In *International conference on offshore mechanics and arctic engineering*, volume 84409, pp. V008T08A005. American Society of Mechanical Engineers, 2020.

Deo, I. K., Gao, R., and Jaiman, R. Combined space–time reduced-order model with three-dimensional deep convolution for extrapolating fluid dynamics. *Physics of Fluids*, 35, 2023.

Eivazi, H., Veisi, H., Naderi, M. H., and Esfahanian, V. Deep neural networks for nonlinear model order reduction of unsteady flows. *Physics of Fluids*, 32, 2020.

Fukami, K., Fukagata, K., and Taira, K. Assessment of supervised machine learning methods for fluid flows. *Theoretical and Computational Fluid Dynamics*, 34:497–519, 2020.

Ghasemian, M., Ashrafi, Z. N., and Sedaghat, A. A review on computational fluid dynamic simulation techniques for darrieus vertical axis wind turbines. *Energy Conversion and Management*, 149:87–100, 2017.

Goodfellow, I., Pouget-Abadie, J., Mirza, M., Xu, B., Warde-Farley, D., Ozair, S., Courville, A., and Bengio, Y. Generative adversarial networks. *Communications of the ACM*, 63:139–144, 2020.

Halder, R., Eiximeno, B., and Lehmkuhl, O. Reduced-order modeling of large-scale turbulence using koopman β -variational autoencoders. *Physics of Fluids*, 38(1), 2026.

Hasegawa, K., Fukami, K., Murata, T., and Fukagata, K. Machine-learning-based reduced-order modeling for unsteady flows around bluff bodies of various shapes. *Theoretical and Computational Fluid Dynamics*, 34:367–383, 2020.

He, K., Zhang, X., Ren, S., and Sun, J. Identity mappings in deep residual networks. In *European conference on computer vision*, pp. 630–645. Springer, 2016.

Hemmasian, A. and Farimani, A. B. Reduced-order modeling of fluid flows with transformers. *Physics of Fluids*, 35, 2023.

Hochreiter, S. and Schmidhuber, J. Long short-term memory. *Neural computation*, 9(8):1735–1780, 1997.

Hu, E. J., Shen, Y., Wallis, P., Allen-Zhu, Z., Li, Y., Wang, S., Wang, L., Chen, W., et al. Lora: Low-rank adaptation of large language models. *ICLR*, 1(2):3, 2022.

Kipf, T. N. and Welling, M. Semi-supervised classification with graph convolutional networks. In *International Conference on Learning Representations (ICLR)*, 2017.

Kohl, G., Chen, L.-W., and Thürey, N. Benchmarking autoregressive conditional diffusion models for turbulent flow simulation. *Neural Networks*, pp. 108641, 2026.

Koopman, B. O. Hamiltonian systems and transformation in hilbert space. *Proceedings of the National Academy of Sciences*, 17:315–318, 1931.

Krizhevsky, A., Sutskever, I., and Hinton, G. E. Imagenet classification with deep convolutional neural networks. In *Advances in Neural Information Processing Systems*, volume 25, pp. 1097–1105, 2012.

Kutz, J. N., Brunton, S. L., Brunton, B. W., and Proctor, J. L. *Dynamic Mode Decomposition: Data-Driven Modeling of Complex Systems*. SIAM - Society for Industrial and Applied Mathematics, 2016.

Lee, S. and You, D. Data-driven prediction of unsteady flow over a circular cylinder using deep learning. *Journal of Fluid Mechanics*, 879:217–254, 2019.

Li, Z., Kovachki, N., Azizzadenesheli, K., Liu, B., Bhattacharya, K., Stuart, A., and Anandkumar, A. Fourier neural operator for parametric partial differential equations. In *International Conference on Learning Representations (ICLR)*, 2021.

Loshchilov, I. and Hutter, F. Decoupled weight decay regularization. *arXiv preprint arXiv:1711.05101*, 2017.

Lu, L., Jin, P., Pang, G., Zhang, Z., and Karniadakis, G. E. Learning nonlinear operators via deepnet based on the universal approximation theorem of operators. *Nature Machine Intelligence*, 3(3):218–229, 2021.

Lusch, B., Kutz, J. N., and Brunton, S. L. Deep learning for universal linear embeddings of nonlinear dynamics. *Nature Communications*, 9, 2018.

Maulik, R., Lusch, B., and Balaprakash, P. Reduced-order modeling of advection-dominated systems with recurrent neural networks and convolutional autoencoders. *Physics of Fluids*, 33, 2021.

Morimoto, M., Fukami, K., Zhang, K., and Fukagata, K. Generalization techniques of neural networks for fluid flow estimation. *Neural Computing and Applications*, 34: 3647–3669, 2021.

Nayak, I., Chakrabarti, A., Kumar, M., Teixeira, F. L., and Goswami, D. Temporally-consistent koopman autoencoders for forecasting dynamical systems. *Scientific Reports*, 15, 2025.

Paszke, A., Gross, S., Massa, F., Lerer, A., Bradbury, J., Chanan, G., Killeen, T., Lin, Z., Gimelshein, N., Antiga, L., et al. Pytorch: An imperative style, high-performance deep learning library. *Advances in neural information processing systems*, 32, 2019.

Ronneberger, O., Fischer, P., and Brox, T. U-net: Convolutional networks for biomedical image segmentation. In *International Conference on Medical image computing and computer-assisted intervention*, pp. 234–241. Springer, 2015.

Sanchez-Gonzalez, A., Godwin, J., Pfaff, T., Ying, R., Leskovec, J., and Battaglia, P. W. Learning to simulate complex physics with graph networks. In *Proceedings of the 37th International Conference on Machine Learning (ICML)*, 2020.

Slotnick, J., Khodadoust, A., Alonso, J., Darmofal, D., Gropp, W., Lurie, E., and Mavriplis, D. Cfd vision 2030 study: A path to revolutionary computational aero-sciences. 2014.

Srinivasan, P. A., Guastoni, L., Azizpour, H., Schlatter, P., and Vinuesa, R. Predictions of turbulent shear flows using deep neural networks. *Physical Review Fluids*, 4, 2019.

Takeishi, N., Kawahara, Y., and Yairi, T. Learning koopman invariant subspaces for dynamic mode decomposition. In *Advances in Neural Information Processing Systems 30*, pp. 1130–1140, 2017.

Vaswani, A., Shazeer, N., Parmar, N., Uszkoreit, J., Jones, L., Gomez, A. N., Kaiser, Ł., and Polosukhin, I. Attention is all you need. In *Advances in Neural Information Processing Systems (NeurIPS)*, volume 30, 2017.

Wang, R., Kashinath, K., Mustafa, M., Albert, A., and Yu, R. Towards physics-informed deep learning for turbulent flow prediction. *Proceedings of the 26th ACM SIGKDD International Conference on Knowledge Discovery & Data Mining*, 2019.

Woo, S., Park, J., Lee, J.-Y., and Kweon, I. S. Cbam: Convolutional block attention module. In *Proceedings of the European conference on computer vision (ECCV)*, pp. 3–19, 2018.

Wu, T., Maruyama, T., and Leskovec, J. Learning to accelerate partial differential equations via latent global evolution. In *Advances in Neural Information Processing Systems (NeurIPS)*, 2022.

Wu, X., Qiu, X., Gao, H., Hu, J., Yang, B., and Guo, C. K²VAE: A koopman-kalman enhanced variational autoencoder for probabilistic time series forecasting. In *Forty-second International Conference on Machine Learning*, 2025.

Wu, Y. and He, K. Group normalization. In *Proceedings of the European conference on computer vision (ECCV)*, pp. 3–19, 2018.

Zhou, H. and Cheng, S. Improving long-term autoregressive spatiotemporal predictions: a proof of concept with fluid dynamics. *Computer Methods in Applied Mechanics and Engineering*, 447:118332, 2025.

A. Data Details

All models were trained on the public data from (Kohl et al., 2026). For a thorough comparison, we used the exact same split in terms of train/evaluation. The incompressible model was trained on all the sequences with Reynolds numbers in the $[200, 900]$ interval with a step of 10, and evaluated on the $Inclow = [100, 200]$, $Inchigh = [900, 1000]$ extreme intervals. The transonic model was also trained on the sequences with Mach numbers in the $[0.53, 0.54, \dots, 0.62, 0.63] \cup [0.69, 0.70, \dots, 0.89, 0.90]$ and evaluated on the sequences with $Tra_{ext} = [0.50, 0.51, 0.52]$, $Tra_{int} = [0.66, 0.67, 0.68]$ for 60 time steps and $Tra_{long} = [0.64, 0.65]$ for 240 time steps. The main difference in training and loading the data, as mentioned in Section 6.1 is we treat them in an exhaustive manner. We follow the same stride (a sub-sampling factor of 2), but we load the data such that the previous sequence’s prediction can be initial conditions for the following sequence.

Moreover, we used a different structure. The original Diffusion Model was using a simple tensor with multiple channels, each of them representing a different variable (v_x, v_y , etc.). For expressiveness we used TensorDicts, which are PyTorch’s (Paszke et al., 2019) version of dictionaries, where the values are tensors. Each of the channels from the original formulation was translated into a specific variable.

B. Implementation and Model Details

The entire model is implemented and trained using PyTorch (Paszke et al., 2019). All weights in the architecture were optimized using AdamW (Loshchilov & Hutter, 2017) with $\beta_1 = 0.9$ and $\beta_2 = 0.999$. The learning rate follows a Cosine Warm-up schedule, linear increasing for the first 20 epochs from 0.0 to 5×10^{-4} , then decreasing on a cosine curve to 10^{-5} for the following 180 epochs, making it 200 epochs in total for training, with a batch size of 64.

We also follow an end-to-end training procedure, learning the encoder, operator and decoder simultaneously. While testing different architectures and training schemes, we have experimented with curriculum learning too. As the model can be rather complex, especially for large latent dimensionality, while the data, more specifically the transonic flow, can be very chaotic and rough, we tried training the Auto-Encoder’s core (encoder and decoder) for the first 50 epochs alone, freezing the operator’s side, as we first wanted to build a smooth manifold for the data. For the following 100 epochs, we have frozen the encoder and decoder and only trained the operator. Finally, for the remaining epochs, we fine-tuned them together. However, this proved challenging as regularizing the latent space was not as straightforward as expected, leaving the linear operator to struggle.

Our model follows a modular *encoder–latent–dynamics–decoder* design, combining convolutional feature extraction with physics-conditioned Koopman operators for latent-space temporal evolution. The architecture is specifically designed for stability, interpretability, and robustness in strongly conditioned fluid dynamics regimes.

B.1. Encoder Architecture

The spatial encoder is a convolutional residual encoder operating on input fields augmented with explicit coordinate information. For each input snapshot of shape $C \times H \times W$, two additional coordinate channels corresponding to normalized spatial coordinates are concatenated, resulting in $C + 2$ input channels. This coordinate injection enables the model to reason about absolute spatial position without relying on implicit convolutional biases.

The encoder backbone begins with an initial 3×3 convolution, followed by a sequence of pre-activation residual blocks (He et al., 2016) with Group Normalization (Wu & He, 2018) and SiLU activations. Each resolution level consists of one downsampling residual block with stride 2, and one refinement residual block with stride 1.

We use three resolution levels with channel widths $[64, 128, 256]$, leading to an effective downsampling factor of $2^3 = 8$. All convolutional and linear layers in the encoder employ spectral normalization, which we found crucial for stabilizing gradients in downstream Koopman dynamics learning.

At the lowest spatial resolution, we apply a Convolutional Block Attention Module (CBAM) (Woo et al., 2018), consisting of sequential channel-wise and spatial attention. This allows the encoder to focus on dynamically active regions such as vortices while suppressing background noise.

The resulting feature map is flattened and projected into a latent representation via a linear layer. This latent representation significantly improves numerical stability of the Koopman operator. When late fusion conditioning is enabled, the flattened spatial features are concatenated with a physics embedding before the final projection.

Conditioning and Physics Parameter Embeddings Physical parameters (e.g. Reynolds number, Mach number, forcing terms) are incorporated through radial basis function (RBF)-style expansions, mapping low-dimensional scalars into higher-dimensional embeddings. The expansion type is configurable and shared across encoder, decoder, and dynamics modules. During training, small Gaussian noise can be injected into the conditioning variables to improve robustness to discretization artifacts and sparse parameter sampling.

B.1.1. TEMPORAL HISTORY ENCODER

For scenarios involving multiple input timesteps, we introduce a history encoder that aggregates temporal context before latent evolution. Each timestep is independently encoded using the convolutional encoder backbone, producing a sequence of latent vectors. These vectors are then processed by a Transformer encoder (Vaswani et al., 2017) with sinusoidal positional encodings. The Transformer output is averaged across time to obtain a single latent context vector, which serves as the initial condition for the Koopman dynamics. This design allows the model to capture temporal correlations without explicitly unrolling convolutional operations over time.

B.2. Decoder Architecture

The decoder mirrors the encoder structure in reverse, reconstructing spatial fields from the latent state. The latent vector is first linearly expanded and reshaped into a low-resolution feature map. Upsampling proceeds through a sequence of resolution levels [256, 128, 64], each consisting of a conditioned residual block, and a resize-convolution upsampling block (nearest-neighbor upsampling followed by a 3×3 convolution).

To integrate physical parameters, we employ Adaptive Group Normalization (AdaGN) within the decoder residual blocks. Here, scale and shift parameters of the normalization layers are modulated by the physics embeddings, enabling strong, spatially uniform conditioning while preserving convolutional locality. Dropout is applied inside conditioned residual blocks for regularization, using element-wise dropout to avoid suppressing entire physical channels. The final output is produced via a 3×3 convolution mapping back to the original number of physical variables.

B.3. Koopman Dynamics Module

Latent evolution is governed by a physics-conditioned Koopman operator, implemented in either discrete-time or continuous-time form. We consider two Koopman parameterizations:

- Linear mode, where the dynamics are governed by a base linear operator with low-rank, condition-dependent updates predicted by a hyper-network (LORA-style adaptation) (Hu et al., 2022).
- MLP-augmented mode, where a linear operator is supplemented by a nonlinear residual MLP to capture weakly nonlinear effects.

Condition dependence is handled via a hyper-network that predicts operator modifications from the physics embeddings. Stability is explicitly enforced through dissipative initialization, spectral constraints, and, in continuous-time settings, stable numerical integration.

For continuous dynamics, we model $\frac{dz}{dt} = K(\phi)z$, and integrate using a fourth-order Runge–Kutta (RK4) scheme by default, with optional implicit midpoint or Radau IIA solvers for stiff regimes. All implicit solvers internally upcast to *float32* to ensure numerical robustness.

C. Training Objective and Loss Function Details

To ensure that the learned latent dynamics are not only accurate in terms of Euclidean error but also physically consistent, stable, and topologically faithful to the fluid flows, we employ a composite loss function. The total objective $\mathcal{L}_{\text{total}}$ is a weighted sum of reconstruction accuracy, temporal rollout consistency, latent space regularization, and physics-informed constraints:

$$\mathcal{L}_{\text{total}} = \mathcal{L}_{\text{recon}} + \alpha \mathcal{L}_{\text{pred}} + \beta \mathcal{L}_{\text{latent}} + \lambda_{\text{phys}} \mathcal{L}_{\text{phys}} \quad (17)$$

Below, we detail the mathematical formulation of the last two components implemented in our framework.

C.1. Latent Space Consistency

To ensure the latent manifold respects the theoretical properties of the Koopman operator, we enforce structural constraints via $\mathcal{L}_{\text{latent}}$. This includes three specific sub-terms:

1. Forward-Backward Linearity Consistency. A valid Koopman operator must be invertible. If $\mathbf{K}(\Delta t)$ propagates the state forward, $\mathbf{K}(-\Delta t)$ must recover the previous state. This is crucial for dissipative systems to prevent the operator from learning a trivial "shrink-to-zero" solution.

$$\mathcal{L}_{\text{lin}} = \underbrace{\|\mathbf{K}(z_t, \Delta t) - z_{t+1}\|_2^2}_{\text{Forward}} + \underbrace{\|\mathbf{K}(z_{t+1}, -\Delta t) - z_t\|_2^2}_{\text{Backward}}. \quad (18)$$

2. Directional Cosine Similarity. To decouple magnitude errors (decay) from directional errors (dynamics), we enforce alignment between the predicted latent vector update and the true encoder trajectory:

$$\mathcal{L}_{\text{cos}} = 1 - \frac{z_{t+1} \cdot \mathcal{E}(x_{t+1})}{\|z_{t+1}\| \|\mathcal{E}(x_{t+1})\|}. \quad (19)$$

3. Energy Conservation Regularization. Ideally, the "energy" (norm) of the latent state should evolve smoothly. We penalize abrupt changes in the latent norm to encourage smooth trajectories:

$$\mathcal{L}_{\text{energy}} = (\|z_{t+1}\|_2 - \|z_t\|_2)^2. \quad (20)$$

The total latent loss is given by $\mathcal{L}_{\text{latent}} = \mathcal{L}_{\text{lin}} + w_{\text{cos}} \mathcal{L}_{\text{cos}} + \mathcal{L}_{\text{energy}}$.

C.2. Physics-Informed Loss

Standard MSE losses often result in "pacing" errors (phase shift) or blurred edges. We mitigate this using a physics-informed loss $\mathcal{L}_{\text{phys}}$ comprising Sobolev norms and spectral analysis.

Temporal Sobolev Loss (Velocity Matching). Enforces consistency in the time-derivative (velocity) of the flow:

$$\mathcal{L}_{\text{time}} = \left\| \frac{\partial \hat{x}}{\partial t} - \frac{\partial x}{\partial t} \right\|_2^2 \approx \|(\hat{x}_{t+1} - \hat{x}_t) - (x_{t+1} - x_t)\|_2^2. \quad (21)$$

Spatial Sobolev Loss (Structure Matching). Enforces consistency in spatial gradients to preserve sharp edges (e.g., shock waves):

$$\mathcal{L}_{\text{space}} = \|\nabla_x \hat{x} - \nabla_x x\|_2^2 + \|\nabla_y \hat{x} - \nabla_y x\|_2^2. \quad (22)$$

Spectral Consistency Loss. To correct phase errors and ensure the model captures the correct shedding frequencies, we compute the loss in the frequency domain using the Fast Fourier Transform (\mathcal{F}). This term penalizes discrepancies in both amplitude (energy spectrum) and phase:

$$\mathcal{L}_{\text{spectral}} = \||\mathcal{F}(\hat{x})| - |\mathcal{F}(x)|\|_1 + \|\text{Re}(\mathcal{F}(\hat{x})) - \text{Re}(\mathcal{F}(x))\|_2^2 + \|\text{Im}(\mathcal{F}(\hat{x})) - \text{Im}(\mathcal{F}(x))\|_2^2. \quad (23)$$

D. Error Analysis

In this appendix, we provide a detailed quantitative and qualitative comparison between our method and ACDM , focusing on accuracy, stability, and robustness across flow regimes. Beyond aggregate error metrics, we emphasize distributional and temporal error characteristics to better understand when and why our approach outperforms diffusion-based forecasting.

We visualize prediction errors using a combination of time-resolved error curves, error bar plots, and violin plots. Error bars report the mean and standard deviation of normalized ℓ_2 errors across test trajectories, highlighting both average performance and variability. Violin plots are used to capture the full error distribution over space and time, revealing differences in tail behavior and robustness that are not visible from mean metrics alone.

Across all evaluated scenarios, our model exhibits consistently lower variance in prediction error, indicating improved stability under long-horizon rollouts. In particular, the error distributions produced by ACDM show heavier tails, corresponding to

occasional but severe prediction failures, whereas our Koopman-based model yields tighter, more concentrated distributions. This effect is especially pronounced in transonic regimes, where diffusion-based models tend to suffer from mode collapse or over-smoothing.

We further include timestep-sensitivity plots, where the same trained model is evaluated under varying rollout step sizes. These visualizations demonstrate that our continuous-time latent dynamics maintain accuracy across a wide range of timesteps, while ACDM performance degrades significantly when evaluated outside its training resolution. This highlights a key advantage of the continuous-time formulation in terms of temporal generalization.

Finally, spatial error maps are presented to illustrate qualitative differences in failure modes. Our model localizes errors primarily in dynamically active regions such as shocks or vortex cores, while maintaining low background error. In contrast, ACDM exhibits spatially diffuse errors that accumulate over time, consistent with the absence of an explicit latent evolution operator.

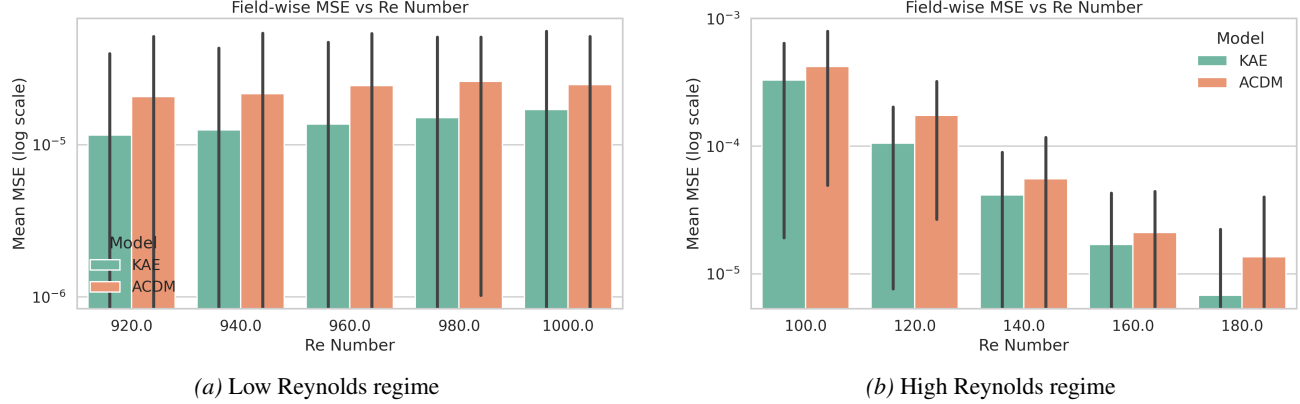


Figure 5. Field-averaged mean squared error (MSE) comparison between KAE and ACDM for incompressible flows. Error bars denote one standard deviation across test trajectories. Our method consistently achieves lower error and reduced variance, with the performance gap widening in the high-Re regime where chaotic dynamics dominate.

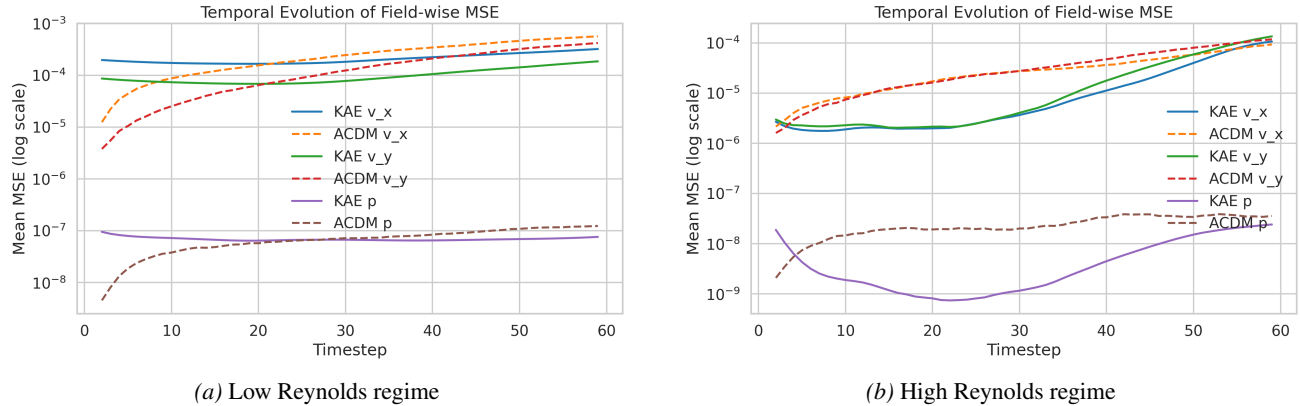


Figure 6. Temporal evolution of field-wise MSE for incompressible flows. Errors are shown on a logarithmic scale. KAE maintains stable error growth over long horizons, while ACDM exhibits accelerated error accumulation, indicative of compounding stochastic prediction drift.

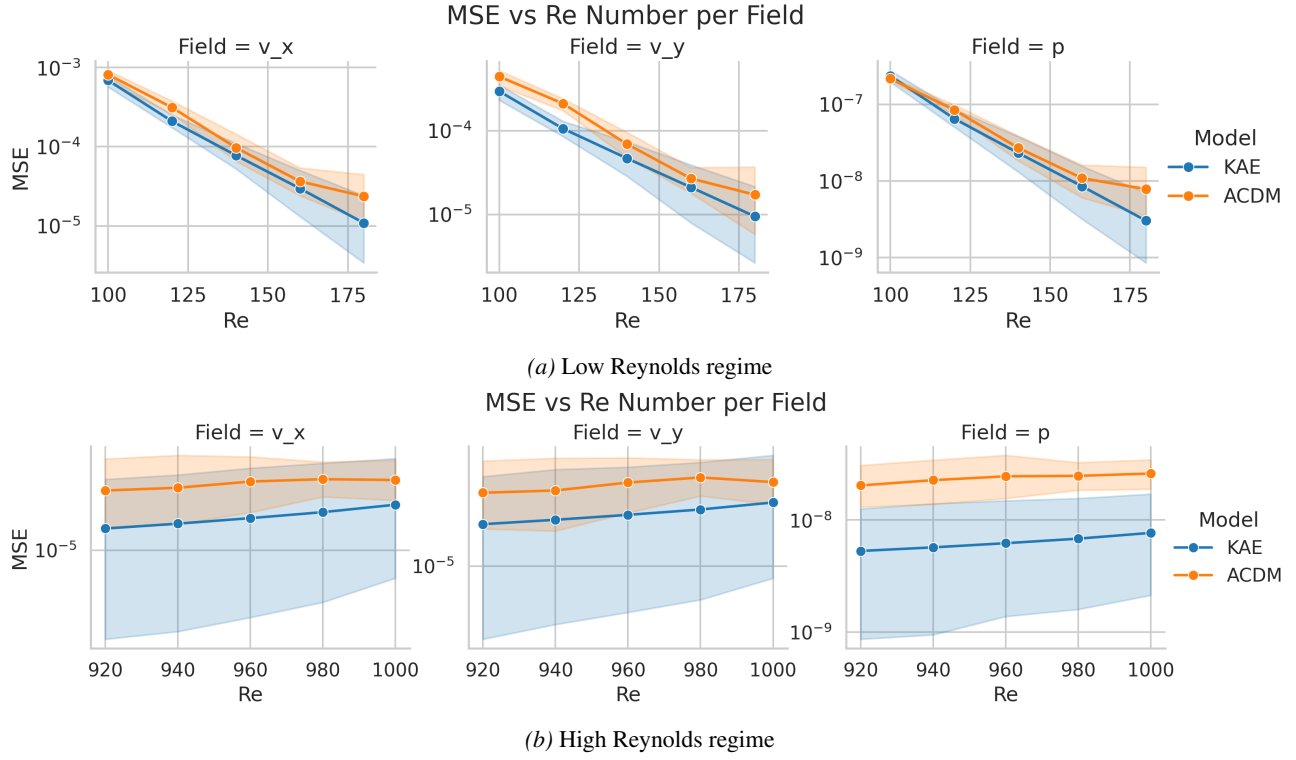


Figure 7. Field-wise MSE as a function of Reynolds number for incompressible flows. Velocity components and pressure are shown separately. KAE exhibits consistently smoother error scaling with Reynolds number, while ACDM shows increased sensitivity and variance, particularly in pressure-dominated regimes.

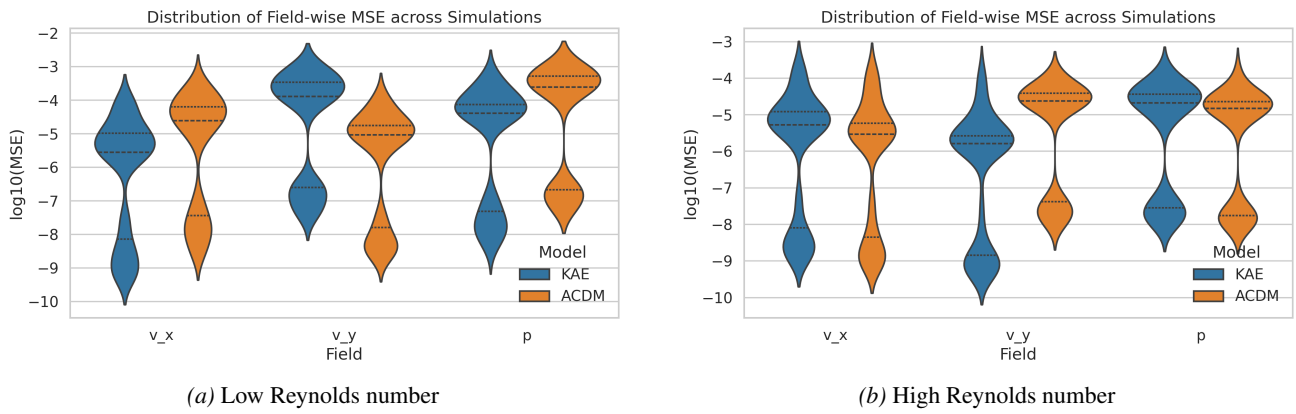


Figure 8. Error distributions under low and high Reynolds number regimes. While both models perform comparably at low Reynolds numbers, ACDM exhibits pronounced heavy-tailed error distributions at high Reynolds numbers. In contrast, KAE maintains controlled variance, demonstrating superior robustness in turbulent regimes.